Korean J. Chem. Eng., **27**(4), 1076-1086 (2010)
DOI: 10.1007/s11814-010-0214-7

Inertial migration and multiple equilibrium positions of a neutrally buoyant spherical particle in Poiseuille flow

Choeng Ryul Choi* and Chang Nyung Kim,***,†**

*Department of Mechanical Engineering, College of Engineering, Kyung Hee University, Yongin 446-701, Korea
**College of Engineering, Kyung Hee University, Yongin 446-701, Korea
***Industrial Liaison Research Institute, Kyung Hee University, Yongin 446-701, Korea
(*Received 24 February 2010 • accepted 29 March 2010*)

Abstract−The radial migration of a single neutrally buoyant particle in Poiseuille flow is numerically investigated by direct numerical simulations. The simulation results show that the Segré and Silberberg equilibrium position moves towards the wall as the Reynolds number increases and as the particle size decreases. At high Reynolds numbers, inner equilibrium positions are found at positions closer to the centerline and move towards the centerline as the Reynolds number increases. At higher Reynolds numbers, the Segré and Silberberg equilibrium position disappears and only the inner equilibrium position exists. We prove that the inner annuluses in the measurements of Matas, Morris & Guazzelli (*J. Fluid Mech.* **515**, 171-195, 2004) are not transient radial positions, but are real equilibrium positions. The results on the inner equilibrium positions and unstable equilibrium positions are new and convince us of the existence of multiple equilibrium radial positions for neutrally buoyant particles.

Key worlds: Segré and Silberberg Effect, Particle Migration, Suspensions, Multiple Equilibrium Positions, Fluid-particle Interaction

INTRODUCTION

Inhomogeneous radial distributions of particles in suspensions flowing through a tube have always been of great interest in both biological and non-biological fields because of the importance of radial migration phenomena in suspension rheology [1,2]. Such a phenomenon is due to the small inertia and wall effect, which cause particle migration across the streamlines of an undisturbed laminar flow [3]. The quantitative experimental evidence of the radial migration was first reported by Segré and Silberberg [1,4] who performed experiments with a dilute suspension of spherical particles in Poiseuille flow through a tube at Reynolds numbers Re=2-700 ($Re=U_{max}R/\nu$ where U_{max} is the maximum velocity, R is the tube radius, and ν is the kinematic viscosity). They found that the particles migrate to an equilibrium radial position of about 0.6 tube radius, irrespective of the radial positions at which the particles are released at the entry. This phenomenon, termed the tubular pinch effect (or the Segré-Silberberg effect), has had a great influence on studies of particle migration and lift in tube flow.

Following their works, a number of experimental studies were performed in several flow configurations (vertical or horizontal flows and channel or tube flows) and with different particle properties (neutrally or non-neutrally buoyant particles) [5-15]. These studies confirmed the Segré and Silberberg's observations and also showed that the general behavior of particles depends strongly on flow configurations and particle properties. For example, these experiments showed that a neutrally buoyant particle in Poiseuille flow stays at the initial radial position at very small Reynolds numbers, migrates to an equilibrium radial position between the centerline and the wall at finite Reynolds numbers, as well as that the equilibrium radial position shifts towards the wall when the Reynolds number is increased and towards the centerline when the particle diameter is increased. Han et al. [16] confirmed that the Segré-Silberberg effect is a very robust phenomenon that is observable for volume fractions up to φ=0.2.

In addition to experimental studies, analytical studies of the lift force, which causes the particle to migrate transversely, were performed using a matched asymptotic expansion method [17,18]. Although these studies explained some of the physics of the Segré-Silberberg effect in the case of non-neutrally buoyant particles, they cannot explain Segré-Silberberg's observations for neutrally buoyant particles. Later, Ho and Leal [2] and Schonberg and Hinch [19] predicted most of the experimental observations for neutrally and non-neutrally buoyant particles in linear or quadratic flow using a regular perturbation method including the influence of the walls and the quadratic nature of the non-perturbed fluid velocity. Schonberg and Hinch [19] calculated the force on a neutrally buoyant particle in two-dimensional quadratic flow for channel Reynolds numbers ($Re_c=U_{max}l/\nu$ where l is the channel width) up to 150 by integrating the solution of the matched asymptotic expansion problem in Fourier space. Later, Asmolov [20] extended this method to channel Reynolds numbers up to 3,000. It should be noted that in order for these theories to be valid, the particle scale Reynolds number must be very small: $Re_p=Re_c(d/l)^2<<1$ where d is the particle diameter. This limitation makes it difficult to apply these analytical methods to practical problems where the particle scale Reynolds number is finite. Besides, since these analytical calculations are made for plane Poiseuille flow, they cannot capture the possible influence of curvature effects in tube flow.

†To whom correspondence should be addressed.
E-mail: cnkim@khu.ac.kr

Since a two-dimensional finite-element scheme based on unstructured body-fitted moving grids was first introduced by Hu et al. [21], several direct numerical simulations of particle migration were performed for Couette flows and plane Poiseuille flows [22-25]. In particular, Patankar et al. [23] and Wang and Joseph [25] obtained correlations of the lift force for a single circular particle in plane Poiseuille flow by processing numerical data. However, the results from two-dimensional simulations are difficult to compare with experimental results because the majority of the experiments are for spherical particles in circular tube flows. In the two-dimensional simulations, the equilibrium radial position shifts towards the channel centerline, while in the experiments it shifts towards the wall as the Reynolds number is increased. There have been few studies which simulate the radial migration of a neutrally buoyant particle in Poiseuille flow [26].

Recently, very interesting observations were reported by Matas et al. [27,28] who measured radial migration of dilute suspensions of neutrally buoyant spherical particles in pipe flows at elevated Reynolds numbers. They found that a single equilibrium radial position (the Segré and Silberberg annulus or outer annulus) was observed which moved towards the wall as the Reynolds number increased in the range of 67 to 350. Another annulus (inner annulus) closer to the centerline, not predicted in the analytical studies using the asymptotic theories, was observed at about 0.5±0.2 times the tube radius for elevated Reynolds numbers (Re≥600). As the Reynolds number increased (Re≥1,650), the outer annulus disappeared and only the inner annulus was clearly observed. They questioned whether this inner annulus corresponds to a true zero of the lift force or is a transient feature, observed only when the entrance length is longer than the system. However, they did not exclude the possibility that the inner annulus is a real equilibrium radial position not captured by the asymptotic theories [20]. The existence of multiple equilibrium radial positions has been confirmed for non-neutrally buoyant particles in plane Poiseuille flows [23,24,29], but not for neutrally buoyant particles in Poiseuille flows. The observations of Matas et al. [27,28] prompt us to consider the possibility of multiple equilibrium radial positions for neutrally buoyant particles in Poiseuille flows. The existence of multiple equilibrium radial positions for neutrally buoyant particles in tube flow has remained an open question.

The present work focuses on the radial migration of a neutrally buoyant spherical particle in Poiseuille tube flow. The radial migration is numerically investigated with direct numerical simulations. The radial lift forces and velocities with radial positions are calculated and the equilibrium radial positions are obtained with Reynolds numbers. To date, only few studies have simulated the radial migration of a neutrally buoyant particle in Poiseuille flow through a tube at elevated Reynolds numbers. In the present work, numerical simulations are extended to high Reynolds numbers up to 1,500, matching the experimental conditions under which multiple equilibrium radial positions were observed by Matas et al. [27,28]. Our simulation results are compared with previous experimental observations and with analytical predictions for plane Poiseuille flow. The simulation results at elevated Reynolds numbers provide a clue as to whether the inner annulus is only a transient radial position where particles are still moving towards the tube wall or another real equilibrium radial position where the radial lift force is zero.

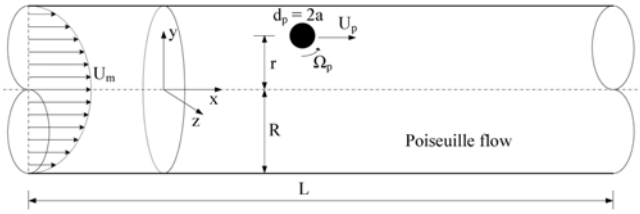

Fig. 1. Schematic of a migration problem of a spherical particle suspended in Poiseuille flow. The particle is neutrally buoyant.

PROBLEM DESCRIPTION, GOVERNING EQUATIONS AND DIMENSIONLESS PARAMETERS

A schematic of the problem considered in the present work is shown in Fig. 1. A neutrally buoyant spherical particle with radius a is freely placed at a radial position r on the x-y plane passing the center of a tube with a radius of R and a length of L. The incompressible Newtonian fluid flows in the positive x-direction, and the flow is laminar.

The governing equations for fluid flow in the problem are

$$\nabla\cdot\mathbf{u}=0 \tag{1}$$

$$\rho_f\left(\frac{\partial\mathbf{u}}{\partial t}+(\mathbf{u}\cdot\nabla)\mathbf{u}\right)=-\nabla p+\mu\nabla^2\mathbf{u} \tag{2}$$

where $\mathbf{u}$ is the flow velocity, ρ_f is the fluid density, p is the pressure, and μ is the molecular viscosity of the fluid.

The translational and rotational motions of the suspended particle satisfy, respectively,

$$m_p\frac{d\mathbf{U}_p}{dt}=\int[-p\mathbf{e}+\tau]\cdot\mathbf{n}d\mathbf{S}=\mathbf{F}_p+\mathbf{F}_\tau \tag{3}$$

$$\mathbf{I}\frac{d\Omega_p}{dt}=\int(\mathbf{x}-\mathbf{X}_p)\times([-p\mathbf{e}+\tau]\cdot\mathbf{n})d\mathbf{S}=\mathbf{T}_p+\mathbf{T}_\tau \tag{4}$$

where m_p is the mass of the particle, $\mathbf{U}_p$ is the translational velocity of the particle, Ω_p is the angular velocity of the particle, $\mathbf{e}$ is the unit tensor. τ is the shear stress tensor and $\mathbf{n}$ is the unit normal vector of the particle surface pointing outward. $\mathbf{S}$ is the surface boundary of the particle. $\mathbf{I}$ is the moment of inertia of the particle and $\mathbf{X}_p$ is the coordinate of the center of mass of the particle. $m_p=\rho_p 4\pi a^3/3$ where ρ_p is the density of the particle and $I=2m_pa^2/5$. The hydrodynamic force $\mathbf{F}$ and moment $\mathbf{T}$ acting on the particle are obtained by integrating the fluid stress over the particle surface. The no-slip condition is satisfied on the particle boundary. The velocity at a point of the particle can be expressed in the following equation:

$$\mathbf{u}=\mathbf{U}_p+\Omega_p\times(\mathbf{x}-\mathbf{X}_p) \tag{5}$$

The velocity profile in the tube Poiseuille flow without the particle is given by

$$u(r)=U_{max}(1-r^2/R^2) \tag{6}$$

where U_{max} is the maximum velocity at the centerline of the tube. r is the radial position and R is the radius of the tube.

Relative motions between the fluid and the particle, which may be characterized by slip velocities, are essential to understanding

the lift force on the particle [24]. The slip translational and angular velocities of the particle at steady state are defined as:

$$U_s = U_f - U_p, \text{ the slip translational velocity} \quad (7)$$

$$\Omega_s = \Omega_p - \Omega_f = \Omega_p + \dot{\gamma}/2, \text{ the slip angular velocity} \quad (8)$$

where U_f and Ω_f are the fluid velocity and angular velocity, respectively, evaluated at the location of the particle center in undisturbed flow. $\dot{\gamma}$ is the local shear rate. The angular velocity discrepancy, defined as $\Omega_s - \Omega_{se}$ where Ω_{se} is the slip angular velocity at equilibrium, changes sign across the equilibrium position just as the lift force does [24].

Here, we introduce dimensionless parameters since they allow us to examine simulation results conveniently [26]. The ratio of the spherical particle radius a (=d/2) to the tube radius R (=D/2) and the dimensionless radial position are defined, respectively, in the following equations:

$$\bar{a} = a/R \text{ and } \bar{r} = r/R. \quad (9)$$

The dimensionless lift is given by

$$\bar{L} = \frac{6\rho_f L}{\pi\mu^2}. \quad (10)$$

The tube Reynolds number (in this paper, termed the Reynolds number) and the particle scale Reynolds number are given by

$$Re = \frac{\rho_f U_{max} R}{\mu} \text{ and } Re_p = Re\left(\frac{d}{D}\right)^2. \quad (11)$$

The undisturbed tube Poiseuille flow without particles is given by Eq. (6). The shear rate at the wall (r=R) is given by $\dot{\gamma}_w = 2U_{max}/R$. We define the velocity $V = 2a\dot{\gamma}_w$ as the characteristic velocity. The shear Reynolds number is

$$Re_s = \frac{\rho_f V(2a)}{\mu} = \frac{\rho_f \dot{\gamma}_w (2a)^2}{\mu} = \frac{8a^2 \rho_f U_{max}}{\mu R}. \quad (12)$$

The dimensionless translational and angular slip velocities are defined as

$$\bar{U}_s = \rho_f U_s (2a)/\mu, \quad \Omega_s = \rho_f \Omega_s (2a)^2/\mu \text{ and } \Omega_{se} = \rho_f \Omega_{se} (2a)^2/\mu. \quad (13)$$

NUMERICAL METHODS

1. Fluid-particle Interaction Scheme

Since the motions of the fluid and particle in the problem are fully coupled to each other, the governing equations have to be solved using two-way coupling in order to determine the hydrodynamic forces acting on the particles and to obtain the motions of both the fluid and the particle without using empirical correlations. Since an approach (called direct numerical simulation, DNS) to simulate the motion of both the fluid and the particles using the arbitrary Lagrangian-Eulerian (ALE) technique was first introduced by [21], the approach has been used in several studies of fluid-particle systems. More details are given by Hu [30] and Hu et al. [31]. Hu and coworkers introduced two schemes: a fully explicit scheme where the particle position and velocity are explicitly updated at each time step, and an explicit-implicit scheme where the particle position and the mesh nodes in the fluid domain are updated explicitly, whereas the particle velocity and the fluid flow field are determined implicitly.

In the present work, we modified some parts of the fully explicit scheme introduced by Hu and coworkers to avoid numerical instabilities and to ensure a strong coupling between the fluid flow and the particle motion in two-way coupling fashion. The calculation procedure for the modified scheme is as follows:

Step 1. Initialize all properties and solution variables.

Step 2. Update the time step.

Step 3. Solve the flow fields ($\mathbf{u}(\mathbf{x}, t_n)$ and $\mathbf{p}(\mathbf{x}, t_n)$) with a typical CFD method, using particle velocities ($\mathbf{U}(t_{n-1})$ and $\Omega(t_{n-1})$) as boundary conditions.

Step 4. Calculate the hydrodynamic force ($\mathbf{F}(t_n)$) and moment ($\mathbf{T}(t_n)$) acting on the particle, using the flow fields ($\mathbf{u}(\mathbf{x}, t_n)$ and $p(\mathbf{x}, t_n)$).

Step 5. Update the particle velocities ($\mathbf{U}(t_n)$ and $\Omega(t_n)$) using the force ($\mathbf{F}(t_n)$) and moment ($\mathbf{T}(t_n)$) by the backward Euler scheme.

Step 6. Update the particle positions and orientations ($\mathbf{X}(t_n)$ and $\theta(t_n)$) using the particle velocities ($\mathbf{U}(t_{n-1})$ and $\Omega(t_{n-1})$). In the case of the fully explicit scheme introduced by Hu and coworkers, the calculation now proceeds to the next time step (go to Step 2) so that Step 7 (below) does not occur.

Step 7. Check the convergence. If $|\mathbf{F}(t_n)/m_p - \dot{\mathbf{U}}(t_{n-1})|$ and $|\mathbf{T}(t_n)/\mathbf{I} - \Omega(t_{n-1})|$ are less than a given tolerance of ε, the calculation proceeds to the next time step and is restarted at the Step 2. If not, another sub-iteration is started at Step 3 with the values predicted by the previous sub-iteration until the convergence criterion is satisfied. Here, $\dot{\mathbf{U}}(t_{n-1})$ and $\Omega(t_{n-1})$ are the translational and angular accelerations predicted at the previous iteration, respectively.

Step 8. The above steps are continued until the end time is reached.

2. Mesh Updating Scheme

The motion of the particle interacting with the fluid flow causes a change in the mesh system in the ALE approach. The mesh system initially designed can be deformed or re-meshed in accordance with the moving particle by a dynamic mesh method in FLUENT (ANSYS, USA). The deforming mesh uses a spring-based method which allows robust mesh deformation under the assumption that the mesh element edges behave like an idealized network of interconnected springs. The re-meshing is adopted to properly treat degenerated cells through the agglomeration of cells that violate a given skewness criterion and the local partition of the agglomerated cells. The mesh is locally updated with new cells satisfying the skewness criterion where the solutions are interpolated from those based on the old cells.

3. Unconstrained and Constrained Simulations

For a neutrally buoyant particle in tube flow, equilibrium can be achieved when the particle migrates to and stays at a radial position (i.e., an equilibrium position $\bar{r}_e$) where steady rectilinear motion may be observed, the acceleration and angular acceleration vanish, and the hydrodynamic lift force is zero. In the present work, unconstrained and constrained simulations are performed to determine the equilibrium radial position and to investigate the radial migration of a neutrally buoyant particle. In the unconstrained simulation, the particle is allowed, with free translation and rotation, to migrate to its equilibrium position, just as in physical experiments. The unconstrained simulation is useful for predicting the particle trajectory. In the constrained simulation first introduced by Patankar et al. [23], the particle is allowed to move only along a line parallel to the axis of the tube and rotate freely while its radial position is

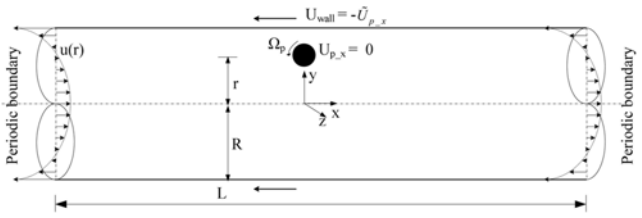

Fig. 2. Computational domain with a periodic boundary in a coordinate system fixed on the particle to simulate the migration of a spherical particle suspended in a Poiseuille flow. The simulations using this approach generate a fully developed parabolic velocity profile, $u(r)=2Q(R^2-r^2)/\pi R^4-\tilde{U}_{p\_x}$, at the left and right boundaries, since the periodic length L of the tube is chosen to be large enough, with L/2a≈150. The pressure at the left boundary is higher than that at the right boundary and the pressure difference is approximately $\Delta p=8\mu LQ/\pi R^4$.

fixed so that it does not translate in the radial direction. When such a constrained motion reaches steady state in which the particle translates in the axial direction at a constant velocity and rotates at a constant angular velocity, a hydrodynamic radial lift force L can be obtained as a function of the radial position with zero radial lift force at the equilibrium position.

The steady state translational and angular velocities as well as the hydrodynamic radial lift force obtained from the constrained simulation are independent of the particle density used. In the present work, we place the particle at (y=r, z=0) (Fig. 1) so that the lift force at steady state is in the y-direction, with no net force in the z-direction. The only components of the particle translational and angular velocity at steady state are U_x and Ω_z, respectively.

4. Computational Domain and Treatment of Boundary Conditions

Numerical simulations are performed in a periodic domain, and a periodic boundary condition is imposed at both ends as shown in Fig. 2. As the particle moves relative to the tube wall, an exact simulation of the system with a fixed set of coordinates requires repeated updates of the computational domain or the use of a very long computational domain to account for the entrance length, which allows the particle to reach steady state.

In the present work, instead of the system with a fixed set of coordinates, we will use a coordinate system fixed on the particle and simulate the particle migration in a periodic domain as shown in Fig. 2, where the particle is always located at the center of the computational domain without being translated in the axial direction. Here, the velocity of the tube wall is set to be $U_{wall}=-\tilde{U}_{p\_x}$ where $\tilde{U}_{p\_x}$ is equivalent to the axial velocity of the particle U_{p_x} in Fig. 1. $\tilde{U}_{p\_x}$ is initially set to be the velocity at the initial center position of the particle in undisturbed Poiseuille flow under a specific flow rate Q and is continuously adjusted during the simulation so that the net axial hydrodynamic force exerted on the particle can be zero. That is, $\tilde{U}_{p\_x(new)}=\tilde{U}_{p\_x(old)}+U_{p\_x}$ where U_{p_x} is the axial velocity of the particle newly derived from Eq. (3) during every sub-iteration (Step 5 of the calculation procedure explained in Section 3.1). Since the velocity of the tube wall is adjusted at every sub-iteration, the flow rate imposed as the boundary condition should also be adjusted, as follows:

$$Q_{(new)}=\frac{(\pi R^2\tilde{U}_{p\_x}-2Q)^2}{4Q} \tag{14}$$

The simulations using the above approach generate a fully developed parabolic velocity profile, $u(r)=2Q(R^2-r^2)/\pi R^4-\tilde{U}_{p\_x}$, at the left and right boundaries since the periodic length L of the tube is chosen to be sufficiently large, with L/2a≈150. The pressure at the left boundary is higher than that at the right boundary, and the pressure difference is approximately $\Delta p=8\mu LQ/\pi R^4$. The calculated steady-state hydrodynamic forces on the particle in the two configurations of Figs. 1 and 2 are identical.

The typical mesh used in the present simulations consists of about 500,000 tetrahedral finite-element cells with refined meshes in the vicinity of the particle and the tube wall. Preliminary calculations have shown that the current mesh system provides sufficient mesh-independent solutions (this issue is not presented in detail in this paper due to limited space). We found that the nodes of the first layer adjacent to the particle surface should be placed as close as possible for stable convergence to a steady state and for reliable prediction.

RESULTS AND DISCUSSION

1. Inertial Migration of a Neutrally Buoyant Particle

Numerical simulations are performed in the computational domain shown in Fig. 2. The diameters of the tube and the particle are 5 cm and 0.75 cm, respectively (the diameter ratio of the particle and tube D/d is 6.67). The periodic length L is 1.1 m, which is chosen to be large enough, with L/d≈150, so that solutions are independent of its value. The fluid density is 1.0 g cm^{-3} and the viscosity is 1.0 poise. The particle suspended in the tube is neutrally buoyant.

The evolutions to equilibrium of the particle which started at two different radial positions $\bar{r}$ =0.2 and 0.8 in the tube flow at Re=50 (U_m=0.2 m s^{-1}) are shown in Fig. 3. These results are obtained from unconstrained simulations where initial flow conditions come from constrained simulations at the above initial radial positions, which are performed using a constrained motion in the radial direction to obtain a fully developed velocity profile. In the unconstrained simulations, the radial motion constraint is released; therefore, the particle can travel to a preferential equilibrium radial position where the lift force is zero. The results show that, no matter where the particle is released, it migrates to an equilibrium radial position of $\bar{r}$ =0.632. The translational and angular velocities finally converge to equilibrium values of U=0.114 m s^{-1} and Ω=5.01 s^{-1}, respectively. The radial migration velocities become zero when the particles reach the equilibrium radial position where the lift force is zero.

The steady-state results at different radial positions calculated in constrained simulations under the above flow conditions are plotted in Figs. 4 and 5. The translational and angular velocities obtained in the constrained simulations are slightly different from the ones evaluated at the particle center in undisturbed flow. However, the differences are relatively prominent as the particle is closer to the wall. The equilibrium radial positions of the particle are the points where the lift force is zero. Two zero-lift points are found in Fig. 4(c). The zero-lift point at the centerline is an unstable equilibrium radial position while the zero-lift point between the centerline and the wall is a stable equilibrium radial position. There are subtle dif-

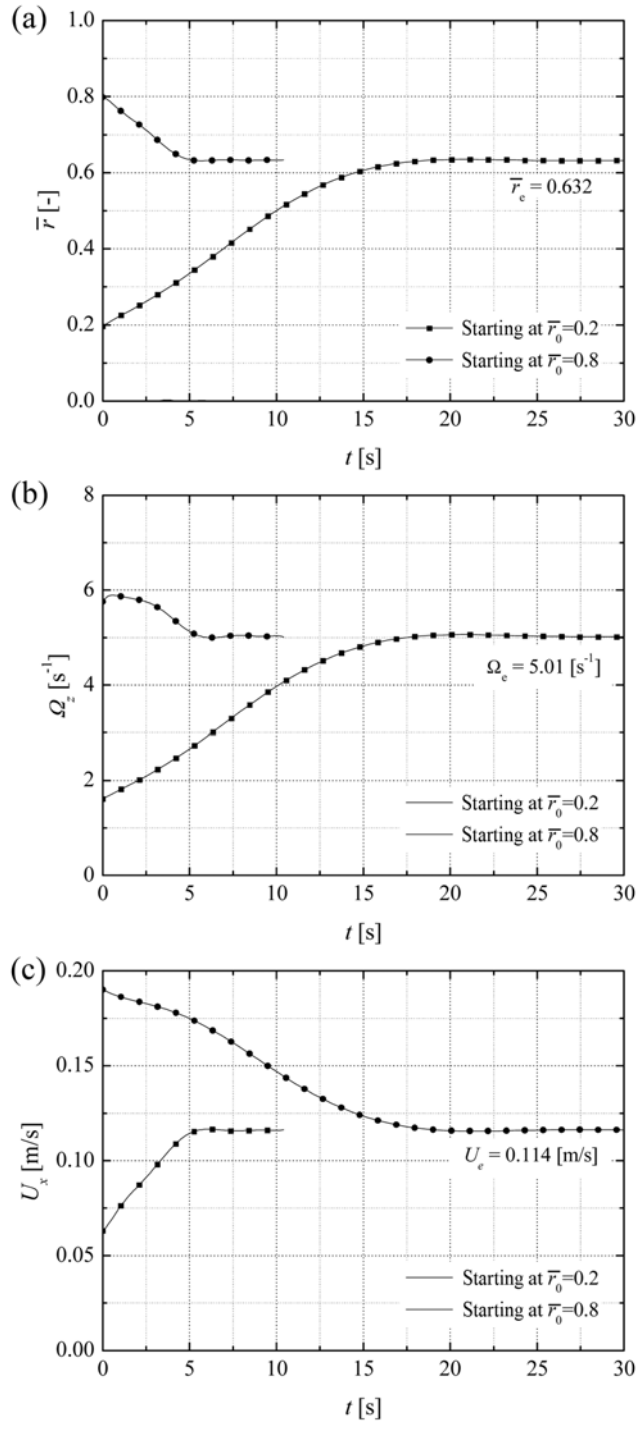

Fig. 3. Evolution to equilibrium of a neutrally buoyant spherical particle with a diameter ratio of D/d=6.67 in the tube flow at Re=50 calculated in an unconstrained simulation. The particle is released at two different radial positions, $\bar{r}$=0.2 and 0.8. (a) radial position, (b) angular velocity, and (c) translational velocity.

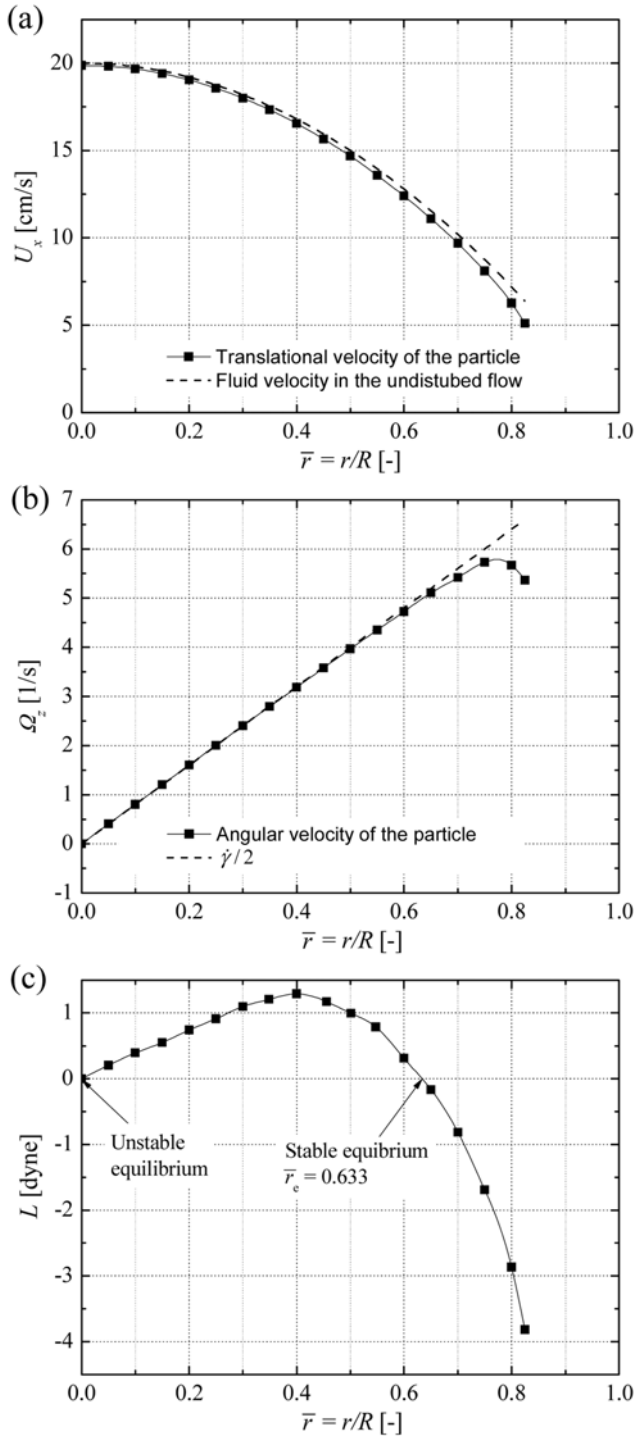

Fig. 4. Steady-state results at different radial positions calculated in constrained simulations for a neutrally buoyant spherical particle with a diameter ratio of D/d=6.67 in the tube flow at Re=50. (a) translational velocity, (b) angular velocity, and (c) lift force on the particle.

ferences between stable and unstable equilibrium radial positions. When a particle is disturbed away from an unstable equilibrium radial position, the particle is driven further away from the unstable equilibrium radial position. On the other hand, when a particle is disturbed away from a stable equilibrium radial position, the lift tends to push the particle back to the stable equilibrium radial position. In the present study, the unstable equilibrium position at the centerline will not be considered. The lift force is positive when the particle is below the stable equilibrium radial position and is negative when it is above. As shown in Fig. 5, the slip velocity is

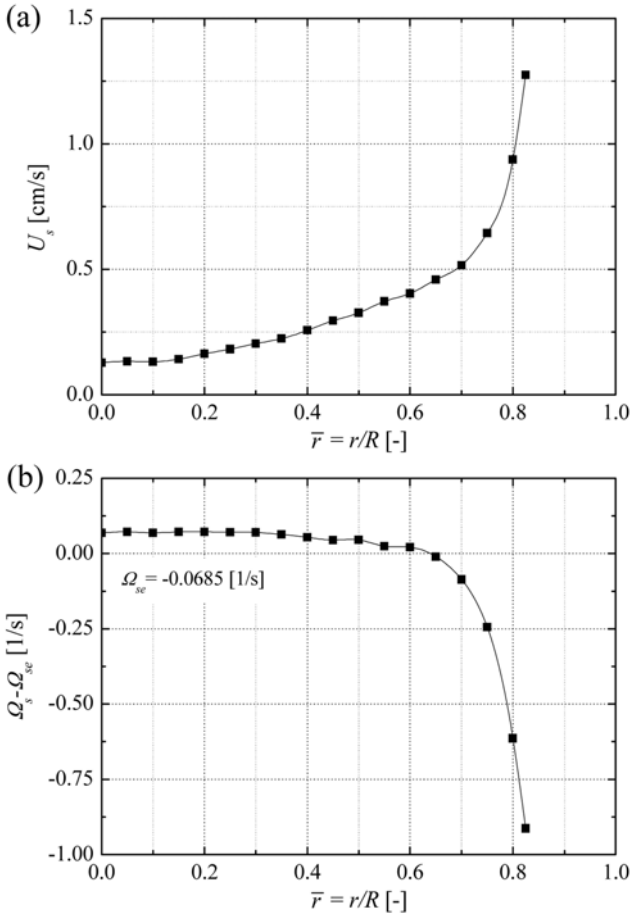

Fig. 5. Slip translational velocities and slip angular velocity discrepancy at different radial positions calculated in constrained simulations for a neutrally buoyant spherical particle with a diameter ratio of D/d=6.67 in the tube flow at Re=50. (a) slip translational velocity and (b) slip angular velocity discrepancy.

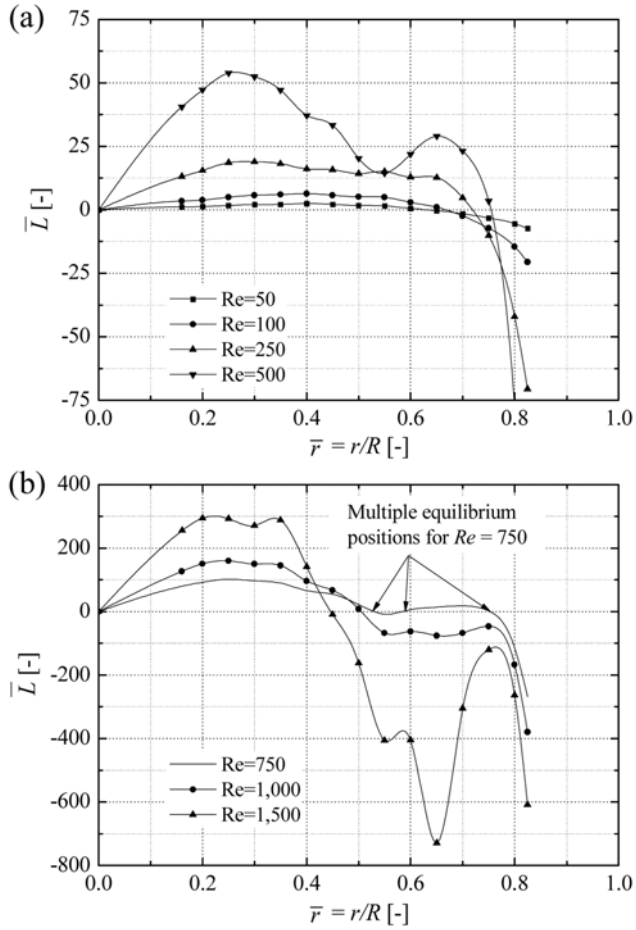

Fig. 6. Lift forces at different radial positions for a particle with diameter ratio D/d=6.67. The four curves in (a) correspond to Re=50, 100, 250, and 500, and the three curves in (b) correspond to Re=750, 1,000, and 1,500, respectively.

always positive, and the sign of the angular slip velocity discrepancy, $\Omega_s - \Omega_{se}$, changes with the sign of the lift force across the equilibrium radial position. Similar results can also be found in the work of Joseph and Ocando [24] who studied the lift force on a circular particle in plane Poiseuille flow perpendicular to gravity. The constrained simulations predict that the translational and angular velocities and the equilibrium radial position are U_e=0.116 m s^{-1}, Ω_e=5.03 s^{-1}, and $\bar{r}_e$=0.633, respectively, which are almost the same as the values calculated in the above unconstrained simulations.

Running the above two sets of simulations, we found that constrained simulations are more economical because it takes much longer for solutions to reach equilibrium in unconstrained simulations. Constrained simulations are also more suitable for this study in that they provide the distributions of the lift force and particle velocities along with the radial positions at steady state. Steady state solutions are important in the study of lift force because of the absence of complicating effects of particle acceleration. Constrained simulations also provide the radial position and velocities of the particle at equilibrium.

The lift forces at different radial positions calculated in constrained simulations are plotted in Fig. 6 for a neutrally buoyant particle with a diameter ratio D/d=6.67 for tube flows ranging from Re=50 to 1,500. The equilibrium radial positions and translational and angular velocities of the particle with the Reynolds number are summarized in Table 1. For Re≤500, a single stable equilibrium radial position exists between the centerline and the wall, and the position moves towards the wall as the Reynolds number increases. For Re=500, the curve of the lift force as a function of the radial position becomes more complicated and a local lift minimum exists at approximately $\bar{r}$ =0.55 between the centerline and the stable equilibrium radial position. For Re=750, three zero-lift points are observed at approximately $\bar{r}$ =0.54, 0.58, and 0.75 between the centerline and the wall. Two zero-lift points at $\bar{r}$ =0.54 and 0.75 are stable equilibrium radial positions and the other at $\bar{r}$ =0.58 is an unstable equilibrium radial position. This result means that neutrally buoyant particles in tube flow can accumulate at multiple radial positions with different translational and angular velocities, as noted in Table 1. The possibility of multiple equilibrium radial positions will be discussed in the next section in detail. As the Reynolds number increases further, two equilibrium radial positions closer to the wall disappear. Only the stable equilibrium radial position close to the centerline exists and it moves towards the centerline, in contrast with the trend for Re=5-500. The equilibrium radial positions for

Table 1. Equilibrium radial positions and translational and angular velocities of a neutrally buoyant spherical particle with the Reynolds number. $\bar{r}_e = r_e/R$, $\overline{U}_e = \rho_f U_e(2a)/\mu$ and $\Omega_e = \rho_f \Omega_e (2a)^2/\mu$ where r_e, U_e and Ω_e are values at equilibrium

D/d		Re								Stable/ Unstable
		5	50	100	250	500	750	1,000	1,500	
6.67	$\bar{r}_e$	0.61	0.63	0.66	0.72	0.75	0.75			Stable
							0.54	0.51	0.45	
							0.58			Unstable
	$\overline{U}_e$	0.9	8.7	16.2	35.2	62.8	95.1	219.5	357.1	Stable
							156.5			
							145.2			Unstable
	Ω_e	0.3	2.8	5.8	14.8	29.7	43.0	41.5	56.6	Stable
							32.2			
							33.9			Unstable
9	$\bar{r}_e$	0.63	0.65	0.68	0.75	0.79	0.81	0.81	0.81	Stable
						0.52	0.50	0.50	0.49	
						0.57	0.65	0.68	0.78	Unstable
	$\overline{U}_e$	0.7	6.2	11.6	24.1	40.8	56.5	74.1	116.1	Stable
						79.8	124.3	165.5	253.5	
						74.2	94.1	118.1	128.9	Unstable
	Ω_e	0.2	1.6	3.4	8.8	18.0	26.7	35.6	51.7	Stable
						12.5	18.2	24.7	36.8	
						13.3	21.7	30.0	49.5	Unstable

Re=1,000 and 1,500 are $\bar{r}$ =0.51 and $\bar{r}$ =0.45, respectively, which are closer to the centerline than the equilibrium radial positions ($\bar{r}$ = 0.61-0.75) calculated for Re=5-500.

To ensure the possible presence of multiple equilibrium radial positions for a neutrally buoyant particle in the tube flow at Re= 750, as shown in Fig. 6, constrained simulations were performed with a smaller particle of diameter ratio D/d=9. The lift forces are plotted in Fig. 7, and the equilibrium radial positions and translational and angular velocities of the particle with the Reynolds number are summarized in Table 1. For Re=50-250, only a single stable equilibrium position exists, which moves towards the wall as the Reynolds number increases. On the other hand, for Re=500-1,500, multiple equilibrium radial positions exist between the centerline and the wall. As the Reynolds number increases, two stable equilibrium radial positions close to the centerline and the wall are slightly shifted towards the centerline and the wall, respectively, and the unstable equilibrium radial position moves slightly towards the wall. These results mean that a neutrally buoyant particle can migrate to a radial position of approximately $\bar{r}$ =0.5 or $\bar{r}$ =0.8 in the tube flows at Re≥ 500. For D/d=9, multiple equilibrium state exists in wide range of Reynolds number (500-1,500) compared to the case of D/d=6.67. It might be due to the influence of the relative curvature effects between the pipe and particle.

The curves of the lift force as a function of the radial position at high Reynolds numbers shown in Figs. 6 and 7 consist of multiple positive and negative slope branches. When the Reynolds number

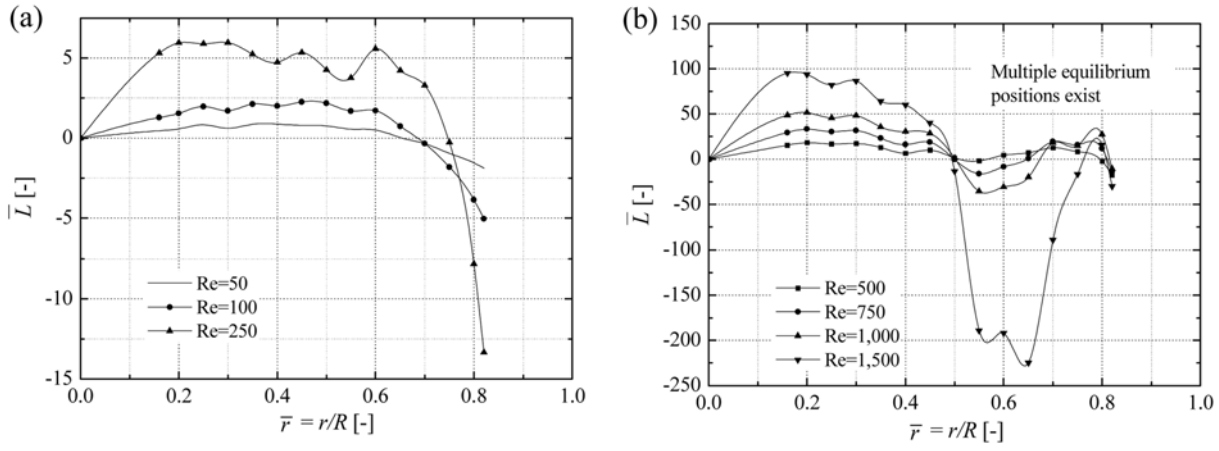

Fig. 7. Lift forces at different radial positions for a particle with diameter ratio D/d=9. The three curves in (a) correspond to Re=50, 100, and 250, and the four curves in (b) correspond to Re=500, 750, 1,000, and 1,500, respectively.

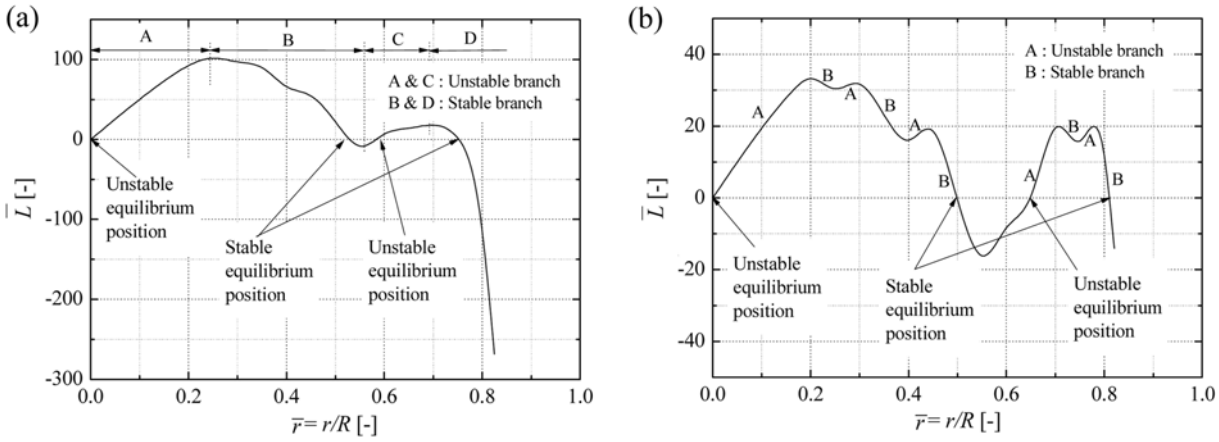

Fig. 8. Lift forces at different radial positions for a particle in tube flow at Re=750. (a) D/d=6.69 (b) D/d=9. The equilibrium radial position of a neutrally buoyant particle is the point where the lift force is zero. There are two stable equilibrium positions and two unstable equilibrium positions.

is small, only a pair of positive and negative slope branches is found. The positive-slope branch is an unstable branch, while the negative-slope branch is a stable branch as indicated in Fig. 8. If a particle is on an unstable branch, the particle experiences an increase in the lift force as the particle migrates to an equilibrium radial position. On the other hand, a particle on a stable branch experiences a decrease in the lift force. Such a complicated distribution of the lift forces at high Reynolds numbers is more apparent for a smaller particle with a ratio of D/d=9, as shown in Fig. 8(b). Similar complicated distributions of the lift force at high Reynolds numbers are found in Asmolov's calculation of the lift force on a small neutrally buoyant sphere in plane Poiseuille flow [20], using matched asymptotic methods. In his Fig. 8, only a pair of positive and negative slope branches are found on the curves for Re=15 and 100. For Re=300, 1,000, and 3,000, two pairs of positive and negative slope branches on the curves are observed and a local minimum of

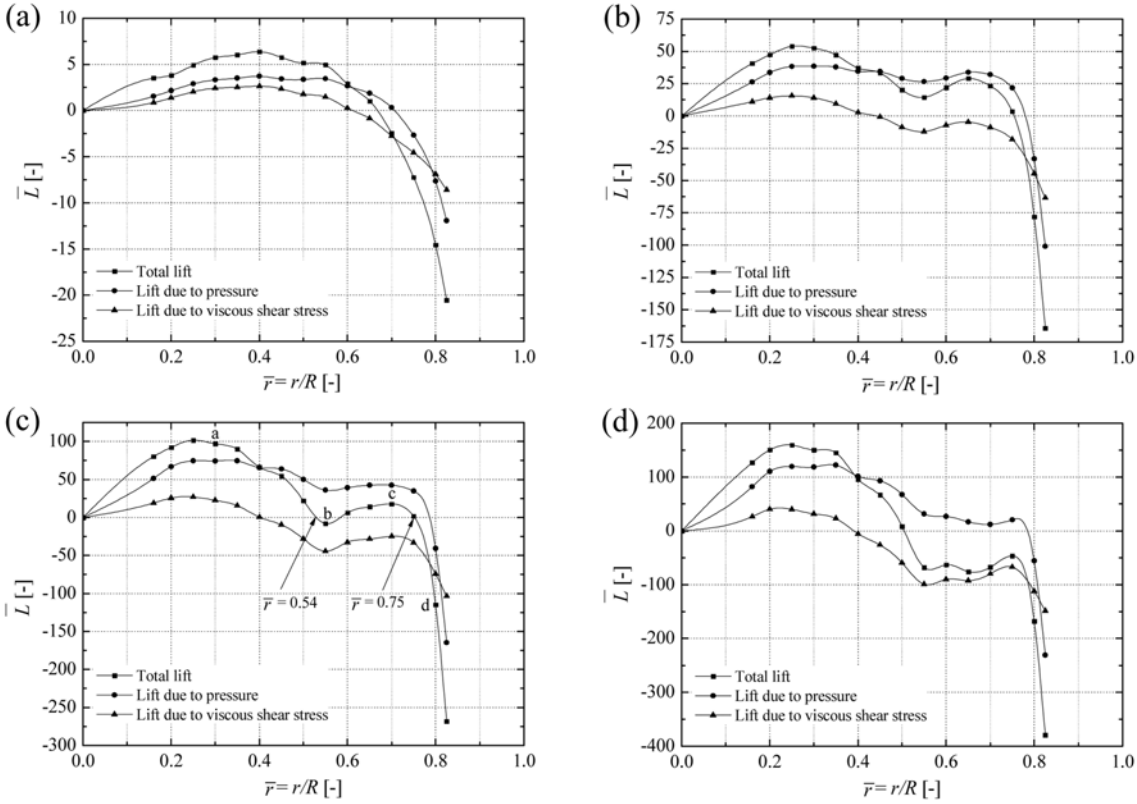

Fig. 9. Contributions of the lift forces due to pressure and viscous shear stress at different radial positions for a particle with diameter ratio D/d=6.67. (a) Re=100, (b) Re=500, (c) Re=750, and (d) Re=1,000. For Re=750, there are two stable equilibrium positions and two unstable equilibrium positions.

the lift force exists. However, his calculations predict only a single equilibrium radial position between the centerline and the wall.

The total lift force acting on a neutrally buoyant particle suspended in tube flow is the sum of the lift forces due to pressure and viscous shear stress on the particle. Both lift forces acting along the y-direction balance at equilibrium radial positions. That is, the total lift force is zero. The contribution of pressure and viscous shear stress to the total lift forces is plotted in Fig. 9 for a particle of D/d=6.67 at Re=100, 500, 750, and 1,000. When the particle is below the equilibrium radial position, the lift force due to pressure is always positive. The lift force due to viscous shear stress changes the sign below the equilibrium radial position. At the equilibrium radial position, the sum of two lift forces is zero; the lift due to pressure is positive, while the lift due to viscous shear stress is negative. This contribution pattern shows that the viscous shear stress plays an important role in determining the equilibrium radial position, since the pressure force pushes the particle to the wall in most regions except for the region very close to the wall, while the shear force changes the sign below the equilibrium radial position. The velocity vectors and pressure distributions at four positions (a-d), indicated in Fig. 9(c), are plotted in Fig. 10. Due to the balance of the lift forces, the particles in (a) and (b) move to a stable equilibrium radial position of $\bar{r}$ =0.54, while the particles in (c) and (d) are shifted to the other stable equilibrium radial position $\bar{r}$ =0.75. The pressure gradient near the particle is significant when the particle is closer to the wall, which leads the lift force due to pressure to be negative in the region close to the wall, that is, the pressure pushes the particle to the centerline.

2. Multiple Equilibrium Radial Positions of Neutrally Buoyant Particles

The variation in the calculated equilibrium radial position as a function of the Reynolds number for each set of particles is presented in Fig. 11, together with results of previous experimental studies [1,27] and an analytical study using asymptotic theory [20]. Segré and Silberberg [1] do not explicitly give the maximum of the histogram for their measurements, but offer the outer radial position where the concentration goes to zero, $r_{lim,}$ and the mean radial position, $\bar{r}$. The value r_{lim} overestimates the equilibrium radial position, while the value $\bar{r}$ certainly underestimates it. The equilibrium radial positions of Segré and Silberberg [1] indicated in Fig. 11 are the values evaluated from $\bar{r}$ /R, where R is the radius of the tube. The error between our results and the measured data results from the broadness of the maximum concentration in their measurements, and is larger at small Reynolds numbers (Re<50) than at large Reynolds numbers. However, it can be seen that our results for large Reynolds numbers (Re>50) are in good agreement with their measurements.

Matas et al. [27] measured lateral migration of dilute suspensions of neutrally buoyant spherical particles (D/d=8-42) in pipe flows at higher Reynolds numbers, Re=67-2,400. They found that a single annulus is observed for Re≤350, and the equilibrium position is shifted closer to the wall as the Reynolds number increases. They reported that a second annulus is observed on the cross-section at a smaller radius (approximately $\bar{r}$ =0.5, spreading from 0.3 to 0.7) for Re>600 when D/d=9-17, and for Re>1,200 when D/d=42. They also reported that, for Re≥1,650, the first annulus close to the wall disappears and that only the second annulus is clearly observed. They tried to explain the second annulus using the change in convexity in the lift force profiles obtained from matched asymptotic methods (Fig. 8 in Asmolov [20]). They argued that, though the particles still tend to leave the centerline, they accumulate in the region of low radial force situated at $\bar{r}$ =0.5±0.2. In their paper, they chose to take the position of the local maximum concentration at larger r to be the Segré and Silberberg annulus when the maximum

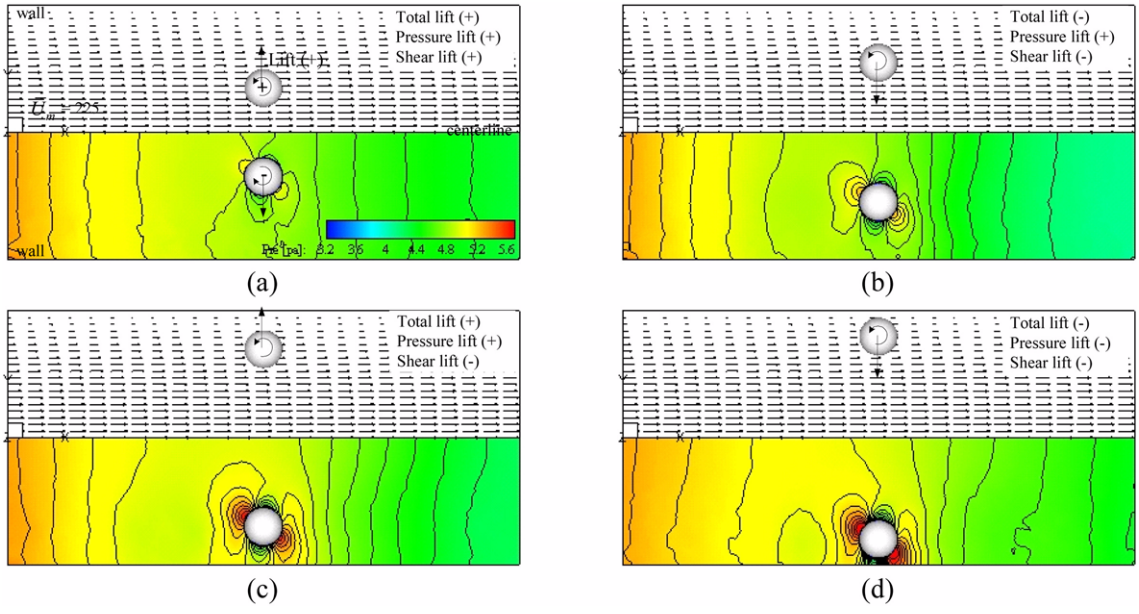

Fig. 10. Velocity vectors and pressure distributions at four different radial positions corresponding to a-d, indicated in Fig. 9(c), for a particle with diameter ratio D/d=6.67 in tube flow at Re=750. For Re=750, there are two stable equilibrium positions ($\bar{r}$=0.54 and 0.75). (a) $\bar{r}$=0.35 ($\bar{U}$=195, Ω=22.7), (b) $\bar{r}$=0.55 ($\bar{U}$=153, Ω=32.7), (c) $\bar{r}$=0.7 ($\bar{U}$=111, Ω=39.6), and (d) $\bar{r}$=0.8 ($\bar{U}$=79, Ω=45.7). The plotted velocity vectors present the vectors converted into the general coordinate system shown Fig. 1.

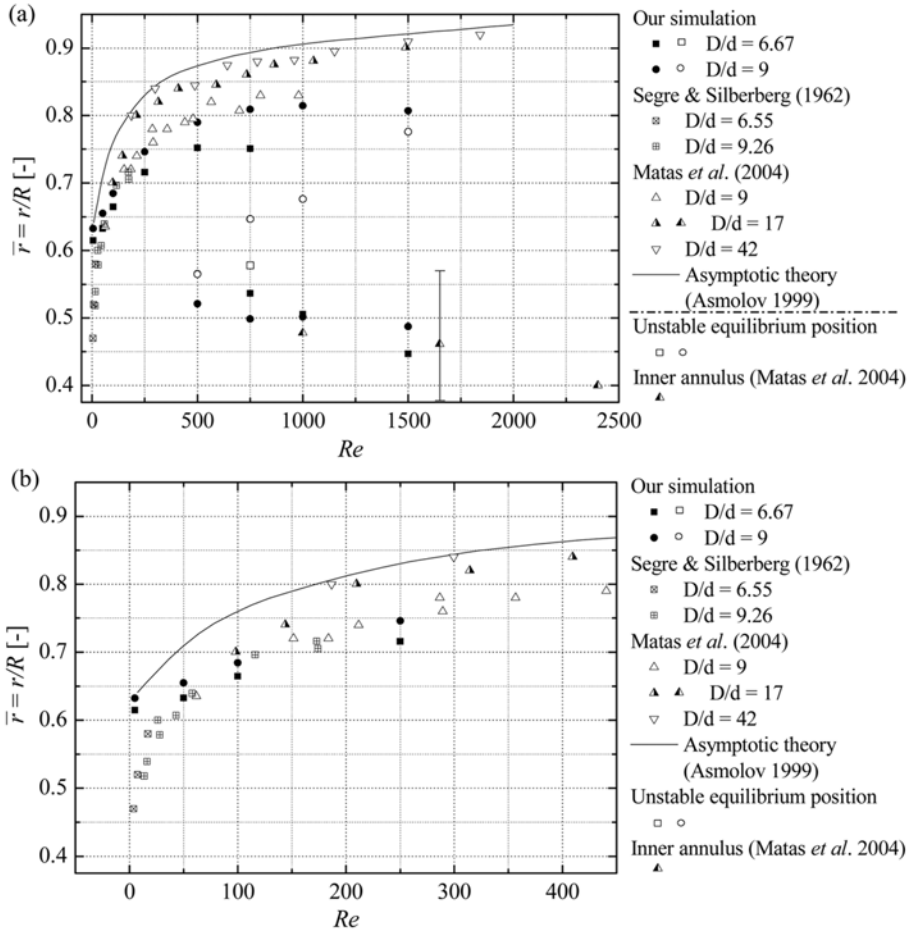

Fig. 11. Equilibrium radial position of a neutrally buoyant spherical particle as a function of Reynolds number for different particle sizes. (b) is an enlargement of part of (a).

concentration corresponds to the position of the second annulus. However, they did not exclude the possibility that the second annulus could be a real equilibrium radial position not captured by the asymptotic theories [20]. We plot both the positions of the maximum and the local maximum in Fig. 11 when multiple annuluses are observed in their measurements. For a particle of D/d=9, the Segré and Silberberg equilibrium positions (which are closer to the wall) calculated in our simulations are in good agreement with theirs. The inner equilibrium radial positions are seen within the same range of $\bar{r}$ =0.5±0.1 in both our results and their measurements. Their paper does not give detailed data related to the inner annulus for other size particles except for D/d=17.

The results of Fig. 11 clearly show that, at a given particle size, the Segré and Silberberg equilibrium radial position (which is closer to the wall) moves towards the wall as the Reynolds number increases, in agreement with the prediction of the asymptotic theory for point particles (the solid line in Fig. 11). At a given Reynolds number, this equilibrium radial position is shifted towards the wall as D/d increases, i.e., as the particle size decreases for a given pipe diameter. This result implies that the smaller the particle is, the closer the equilibrium radial position is to the prediction of the asymptotic theory for point particles. The inner equilibrium radial positions observed for Re=750 when D/d=6.67 and for Re≥500 when D/d=9 are found at closer positions to the centerline than the Segré and Silberberg equilibrium radial positions and move towards the centerline as the Reynolds number increases, in contrast with the Segré and Silberberg equilibrium position. The unstable equilibrium radial position for Re=750 when D/d=6.67 and for Re≥500 when D/d=9 is indicated in Fig. 11 and is shifted towards the wall as the Reynolds number increases. The results related to the inner equilibrium radial positions and the unstable equilibrium radial positions are new and convince us of the existence of multiple equilibrium radial positions for neutrally buoyant particles for certain Reynolds numbers.

We can explain better the remarkable observations in Matas et al. [27] based on our simulation results. For example, the inner annuluses in their measurements are not transient radial positions that occur prior to the Segré and Silberberg equilibrium radial positions (which are closer to the wall), but rather are real equilibrium radial positions where the radial lift forces are zero, as shown in Figs. 6 and 7. The curves of the lift forces in Figs. 6-8 allow us to explain why the concentration in the inner annulus is higher than that in the outer annulus when multiple annuluses are observed in their measurements. The reason is as follows. The particles initially placed between the centerline and the unstable equilibrium radial position finally accumulate in the inner annulus, while the particles between the unstable equilibrium radial position and the wall accumulate in the outer annulus. Therefore, the higher concentration in the inner

annulus results from the much longer distance between the centerline and the unstable equilibrium radial position.

CONCLUSION

The radial migration of a single neutrally buoyant particle in Poiseuille flow has been investigated by direct numerical simulations. Two types of simulations, unconstrained and constrained simulation, have been performed to obtain solutions at equilibrium and both of them have predicted almost the same radial position and translational and angular velocities at equilibrium. Our simulation results are qualitatively and quantitatively in good agreement with the results in experimental and analytical studies.

The simulation results clearly show that, at a given particle size, the Segré and Silberberg equilibrium radial position, which is closer to the wall, moves towards the wall as the Reynolds number increases, in agreement with the prediction of the asymptotic theory for point particles. At a given Reynolds number, this equilibrium radial position is shifted towards the wall as the particle size decreases for a given pipe diameter. This result implies that the smaller the particle is, the closer the equilibrium radial position is to the prediction of the asymptotic theory for point particles. At high Reynolds numbers, the inner equilibrium radial positions are found at closer positions to the centerline than the Segré and Silberberg equilibrium positions, and move towards the centerline as the Reynolds number increases, in contrast with the Segré and Silberberg equilibrium radial position. The unstable equilibrium radial position is shifted towards the wall as the Reynolds number increases. The Segré and Silberberg equilibrium position disappears at higher Reynolds numbers and only an inner equilibrium radial position exists. The contribution to lift force also shows that the viscous shear stress plays an important role in determining the equilibrium radial position at higher Reynolds numbers. The pressure force pushes the particle to the wall in most regions except for the region very close to the wall, while the shear force changes the sign below the equilibrium radial position.

In this study, we have clearly proved that the inner annuluses in the measurements of Matas et al. [27] are not transient radial positions prior to the occurrence of Segré and Silberberg equilibrium positions, but rather are real equilibrium radial positions where the radial lift forces are zero. The results related involving inner equilibrium radial positions and unstable equilibrium radial positions are new and convince us of the existence of multiple equilibrium radial positions for neutrally buoyant particles for certain Reynolds numbers. To the best of our knowledge, this study is the first attempt to prove the possible presence of multiple equilibrium radial positions for neutrally buoyant particles.

REFERENCES

1. G. Segré and A. Silberberg, *J. Fluid Mech.*, **14**, 136 (1962).
2. B. P. Ho and L. G. Leal, *J. Fluid Mech.*, **65**, 365 (1974).
3. F. P. Bretherton, *J. Fluid Mech.*, **14**, 284 (1962).
4. G. Segré and A. Silberberg, *Nature*, **189**, 209 (1961).
5. R. Oliver, *Nature*, **194**, 1269 (1962).
6. H. L. Goldsmith and S. G. Mason, *J. Colloid Sci.*, **17**, 448 (1962).
7. R. Eichhorn and S. Small, *J. Fluid Mech.*, **20**, 513 (1964).
8. R. V. Repetti and E. F. Leonard, *Nature*, **203**, 1346 (1964).
9. R. C. Jeffrey and J. R. A. Pearson, *J. Fluid Mech.*, **22**, 721 (1965).
10. H. Brenner, *Adv. Chem. Eng.*, **6**, 287438 (1966).
11. A. Karnis, H. L. Goldsmith and S. G. Mason, *Can. J. Chem. Eng.*, **44**, 181 (1966).
12. H. L. Goldsmith and S. G. Mason, *The microrheology of dispersions*, in Rheology, Theory and Applications 4, Academic Press, New York (1967).
13. J. S. Halow and G. B. Wills, *AIChE J.*, **16**, 281 (1970).
14. M. Tachibana, *Rheol. Acta*, **12**, 58 (1973).
15. H. Aoki, Y. Kurosaki and H. Anzai, *Bull. JSME*, **22**, 206 (1979).
16. M. Han, C. Kim, M. Kim and S. Lee, *J. Rheol.*, **43**, 1157 (1999).
17. S. I. Rubinow and J. B. Keller, *J. Fluid Mech.*, **11**, 447 (1961).
18. P. G. Saffman, *J. Fluid Mech.*, **22**, 385 (1965).
19. J. A. Schonberg and E. J. Hinch, *J. Fluid Mech.*, **203**, 517 (1989).
20. E. S. Asmolov, *J. Fluid Mech.*, **381**, 63 (1999).
21. H. H. Hu, D. D. Joseph and M. J. Crochet, *Theor. Comput. Fluid Dyn.*, **3**, 285 (1992).
22. J. Feng, H. H. Hu and D. D. Joseph, *J. Fluid Mech.*, **277**, 271 (1994).
23. N. A. Patankar, P. Y. Huang, T. Ko and D. D. Joseph, *J. Fluid Mech.*, **438**, 67 (2001).
24. D. D. Joseph and D. Ocando, *J. Fluid Mech.*, **454**, 263 (2002).
25. J. Wang and D. D. Joseph, *Phys. Fluids*, **15**, 2267 (2003).
26. B. H. Yang, J. Wang, D. D. Joseph, H. H. Hu, T. W. Pan and R. Glowinski, *J. Fluid Mech.*, **540**, 109 (2005).
27. J. P. Matas, J. F. Morris and E. Guazzelli, *J. Fluid Mech.*, **515**, 171 (2004a).
28. J. P. Matas, J. F. Morris and E. Guazzelli, *Oil Gas Sci. Technol.*, **59**, 59 (2004b).
29. T. Ko, N. A. Patankar and D. D. Joseph, *Computers & Fluids*, **35**, 121 (2006).
30. H. H. Hu, *Intl. J. Multiphase Flow*, **22**, 335 (1996).
31. H. H. Hu, N. A. Patankar and M. Y. Zhu, *J. Comput. Phys.*, **169**, 427 (2001).